



1 **Evaluating Simplifications of Subsurface Process** 2 **Representations for Field-scale Permafrost Hydrology Models**

3 Bo Gao, Ethan T. Coon

4 Environmental Sciences Division, Oak Ridge National Laboratory, Oak Ridge, Tennessee, USA

5 *Correspondence to:* Ethan T. Coon (coonet@ornl.gov)

6 **Abstract.** Permafrost degradation within a warming climate poses a significant environmental
7 threat through both the permafrost carbon feedback and damage to human communities and
8 infrastructure. Understanding this threat relies on better understanding and numerical
9 representation of thermo-hydrological permafrost processes, and the subsequent accurate
10 prediction of permafrost dynamics. All models include simplified assumptions, implying a tradeoff
11 between model complexity and prediction accuracy. The main purpose of this work is to
12 investigate this tradeoff when applying the following commonly made assumptions: (1) assuming
13 equal density of ice and liquid water in frozen soil; (2) neglecting the effect of cryosuction in
14 unsaturated freezing soil; and (3) neglecting advective heat transport during soil freezing and thaw.
15 This study designed a set of 62 numerical experiments using the Advanced Terrestrial Simulator
16 (ATS v1.2) to evaluate the effects of these choices on permafrost hydrological outputs, including
17 both integrated and pointwise quantities. Simulations were conducted under different climate
18 conditions and soil properties from three different sites in both column- and hillslope-scale
19 configurations. Results showed that amongst the three physical assumptions, soil cryosuction is
20 the most crucial yet commonly ignored process. Neglecting cryosuction, on average, can cause 10%
21 ~ 20% error in predicting evaporation, 50% ~ 60% error in discharge, 10% ~ 30% error in thaw
22 depth, and 10% ~ 30% error in soil temperature at 1 m beneath surface. The prediction error for
23 subsurface temperature and water saturation is more obvious at hillslope scales due to the presence
24 of lateral flux. By comparison, using equal ice-liquid density has a minor impact on most
25 hydrological variables, but significantly affects soil water saturation with an averaged 5% ~ 15%
26 error. Neglecting advective heat transport presents the least error, 5% or even much lower, in most
27 variables for a general Arctic tundra system, and can decrease the simulation time at hillslope
28 scales by 40% ~ 80%. By challenging these commonly made assumptions, this work provides
29 permafrost hydrology modelers important context for better choosing the appropriate process



30 representation for a given modeling experiment.

31

32 **Copyright Statement.** This manuscript has been authored by UT- Battelle, LLC under Contract
33 No. DE-AC05-00OR22725 with the U.S. Department of Energy. The United States Government
34 retains and the publisher, by accepting the article for publication, acknowledges that the United
35 States Government retains a non-exclusive, paid-up, irrevocable, world-wide license to publish, or
36 reproduce the published form of this manuscript, or allow others to do so, for United States
37 Government purposes. The Department of Energy will provide public access to these results of
38 federally sponsored research in accordance with the DOE Public Access Plan
39 (<http://energy.gov/downloads/doe-public-access-plan>).

40 **1 Introduction**

41 Permafrost describes a state of ground which stays frozen continuously over multiple years, which
42 may cover an entire region (e.g., Arctic tundra) or occur in isolation (e.g., alpine top). From the
43 perspective of scope, permafrost occupies approximately 23.9% (22.79 million km²) of the
44 exposed land area of the northern hemisphere (Zhang et al., 2008), as well as alpine regions and
45 Antarctica in the southern hemisphere. Permafrost areas store a vast amount of organic carbon, of
46 which most is stored in perennially frozen soils (Hugelius et al., 2014). If the organic carbon is
47 exposed due to permafrost thaw, it is likely to decay with microbial activity, releasing greenhouse
48 gas to the atmosphere and exacerbating global warming. In Arctic tundra, permafrost also plays
49 an important role in maintaining water, habitat of wildlife, landscape, and infrastructure (Berteaux
50 et al., 2017; Dearborn et al., 2021; Hjort et al., 2018; Sugimoto et al., 2002). Permafrost
51 degradation may cause significant damage to the local ecosystem, reshape the surface and
52 subsurface hydrology, and eventually influence the global biosphere (Cheng and Wu, 2007;
53 Jorgenson et al., 2001; Tesi et al., 2016; Walvoord and Kurylyk, 2016). Therefore, the occurrent
54 and potential impacts motivate the development of computational models with the goal of better
55 understanding the thermal and hydrological processes in permafrost regions, and consequently
56 predict permafrost thaw accurately.

57 Simulating soil freezing and thaw processes is a challenging task that incorporates mass and energy
58 transfer among atmosphere, snowpack, land surface (perhaps with free water), and a variably
59 saturated subsurface. Several hydrological models with different complexity and applicable scales



60 have been developed to investigate the complicated interactions. A comprehensive review of
61 permafrost models based on empirical and physical representations using analytical and numerical
62 solutions can be found in (Bui et al., 2020; Dall’Amico et al., 2011; Jan et al., 2020; Kurylyk et
63 al., 2014; Kurylyk and Watanabe, 2013; Riseborough et al., 2008). Process-rich models which aim
64 to predict permafrost change through direct simulation of mass and energy transport, such as
65 the Advanced Terrestrial Simulator (ATS; Painter et al., 2016), GEOtop (Endrizzi et al., 2014),
66 CryoGrid 3 (Westermann et al., 2016), PFLOTRAN-ICE (Karra et al., 2014), and SUTRA-ICE
67 (McKenzie et al., 2007), have been demonstrated to describe thermal permafrost hydrology under
68 various climate conditions. Nominally, representing more physical process complexity should
69 improve accuracy, but how much accuracy and at what computational expense (and therefore
70 tradeoff in ability to run larger, or larger ensembles of, simulations) is not always theoretically
71 known. Thus, certain assumptions or simplifications about the system are a significant part of
72 model development.

73 Even in the most process-rich models of permafrost change, three such physics simplifications are
74 often made: representing water at constant density (thereby neglecting the expansion of ice relative
75 to liquid water), neglecting cryosuction of water in unsaturated, partially frozen soils, and
76 neglecting advective heat transport.

77 First, because of the lower density of ice than liquid water, freezing water must expand the volume
78 of the porous media, push liquid water into nearby volume, or otherwise expand the volume
79 occupied by that water. As all of the current set of models operate under the assumption of a rigid
80 solid matrix and thus the absence of mechanical equations describing matrix deformation or frost
81 heave, including this expansion typically results in large pressures that must be offset by grain
82 compressibility or another mechanism. Therefore, the densities of ice and liquid water are
83 frequently assumed equal (e.g., Dall’Amico et al., 2011; Devoie and Craig, 2020; Weismüller et
84 al., 2011). It is uncertain whether this simplification affects predictions of permafrost change and
85 thermal hydrology.

86 Second, cryosuction describes the redistribution of water in partially frozen, unsaturated soils
87 caused by increased matric suction. At the interface of ice and liquid water, negative pressures
88 result in the migration of liquid water toward the freezing front and the subsequent increase of ice
89 content. Several approaches representing cryosuction in models are used (Dall’Amico et al., 2011;
90 Noh et al., 2012; Painter and Karra, 2014; Stuurop et al., 2021), either in an empirical form or



91 physically derived from the generalized Clapeyron equation. Other process-rich models have
92 ignored cryosuction entirely (McKenzie et al., 2007; Viterbo et al., 1999). Dall'Amico et al.
93 (2011), Painter (2011) and Painter and Karra (2014) evaluated their respective Clapeyron equation
94 based cryosuction models in soil column freezing simulations and presented a good match between
95 simulations and laboratory experiments in total water content (liquid and ice). Recently, Stuurop
96 et al. (2021) applied an empirical expression, a physics-based expression, and no cryosuction in
97 simulating soil column freezing process. They compared the simulated results with observations
98 from laboratory experiments. This comparison demonstrated minor differences between empirical
99 and Clapeyron-based cryosuction expressions, but the simulation without cryosuction cannot
100 predict the distribution of total water content in a laboratory-scale soil column. To our knowledge,
101 there is still no literature showing the effect of cryosuction on plot-scale permafrost predictions.
102 Third, heat transport in process-rich models is described using an energy conservation equation,
103 mainly including heat conduction, latent heat exchange, and heat advection. From a continuum-
104 scale perspective, conductive heat transport is expressed in the form of a diffusive term base
105 on Fourier's law. Latent heat exchange accompanies phase change which alters the system enthalpy.
106 Advective heat transport describes the energy exchange caused by the flow of liquid water driven
107 by a hydraulic gradient (i.e., forced convection), which is expressed through an advective term in
108 energy balance equations. Additionally, other mechanisms that control heat transport, such as
109 water vapor movement, thermal dispersion, radiant energy, etc., are neglected by nearly all models
110 of permafrost and are not considered here. Among these heat transport mechanisms, it is
111 commonly recognized that heat conduction predominates heat transport in the subsurface (Nixon,
112 1975). However, there are also studies demonstrating the importance of advective heat transport
113 in permafrost hydrology through field observation analysis or modeling comparison. Such
114 situations where advective heat makes important contributions roughly fall into three categories.
115 The first centers on the development of taliks beneath lakes, ponds, snowmelt water and rainfall
116 induced runoff, or in the existence of supra-/sub-permafrost groundwater flow (e.g., Luethi et al.,
117 2017; McKenzie and Voss, 2013; Rowland et al., 2011). The second focuses on microtopographic
118 features that focus significant amount of water flux through small areas. This includes both low-
119 center ice wedge polygons associated with the formation of thermokarst ponds (e.g., Abolt et al.,
120 2020; Harp et al., 2021) and thermo-erosion gullies (e.g., Fortier et al., 2007; Godin et al., 2014).
121 In these cases, large, focused flows across small spatial scales allow advective heat transport to



122 dominate. The last category includes those studying the construction and maintenance of
123 infrastructure influenced by groundwater flow (e.g., Chen et al., 2020). Thus, these studies focus
124 on either location-specific or scale-limited problems. As McKenzie and Voss (2013) stated,
125 whether heat advection outweighs heat conduction depends on soil permeability, topography, and
126 groundwater availability. Relative to these special cases, we are more interested in to what extent
127 advective heat transport associated with liquid water flow contributes to permafrost hydrologic
128 change in a hillslope-scale or larger Arctic system.

129 To clarify the significant differences in model representations of permafrost, we investigate the
130 influence of including or not including these processes on permafrost change at plot-to-hillslope
131 scales. We take the advantage of the flexibility offered by ATS to express multiple options of
132 process representation to implement this study in numerical experiments. For ice density, we
133 compare simulations with and without differences in ice density relative to water density; for
134 cryosuction, we compare simulations using a Clapyron equation-based expression and excluding
135 the cryosuction effect; and for heat transport, we compare simulations including or neglecting
136 advective heat transport. All comparisons are carried out across a range of Arctic climate
137 conditions and soil properties from three different sites. Both 1D soil-column-scale and 2D
138 hillslope-scale models are considered, in which varying hillslope geometries (i.e.,
139 convergent/divergent hillslope) and aspects (i.e., north/south) are included. The aim of this study
140 is to provide permafrost hydrology modelers with crucial comparisons for better choosing a model
141 representation for a given study by formally considering the tradeoff between model complexity,
142 accuracy, and, at least for one code, performance.

143 **2 Theory**

144 The Advanced Terrestrial Simulator (ATS v1.2) (Coon et al., 2020) configured in permafrost mode
145 (Jan et al., 2018, 2020; Painter et al., 2016) was used to implement all numerical experiments in
146 this study. ATS is a process-rich code developed for simulating integrated surface and subsurface
147 hydrological processes, specifically capable of permafrost applications. It has been shown to
148 successfully compare to observations of seasonal soil freezing and thaw processes at different
149 scales. This includes 1D models of vertical energy transport typical of large-scale flatter regions
150 (Atchley et al., 2015), and 2D models admitting lateral flow and transport in Arctic fens (Sjöberg
151 et al., 2016), and polygonal ground (Jan et al., 2020).



152 The permafrost configuration of ATS comprises coupled water flow and energy transfer within
153 variably saturated soils and at land surfaces, a surface energy balance model describing thermal
154 processes in snow, and a snow distribution module for surface microtopography (Painter et al.,
155 2016). The subsurface system solves a three-phase (liquid, ice, gas), two-component (water vapor,
156 air) Richards-type mass balance equation with Darcy’s law and an advection-diffusion energy
157 balance equation. The surface system includes an overland flow model with diffusion wave
158 approximation, and an energy balance equation with an introduced temperature-dependent factor
159 describing the effect of surface water freezing. The subsurface system and surface system are
160 coupled through the continuity of pressure, temperature, and the corresponding fluxes by
161 incorporating the surface equations as boundary conditions of the subsurface equations (Coon et
162 al., 2020). The evolution of a snowpack and its effect on the surface energy balance is described
163 using an energy balance approach based on a subgrid model concept that includes all major heat
164 fluxes at the land surface. For a more detailed description of the permafrost configuration and
165 implementation in ATS, as well as key mathematical equations, the reader is referred to Painter et
166 al. (2016). Changes in this “most complex” model of permafrost hydrology are enabled by the
167 Arcos multiphysics library leveraged in ATS; this allows the precise model physics to be specified
168 and configured at runtime through the use of a dependency graph describing swappable
169 components in the model physics (Coon et al., 2016).

170 2.1 Ice density

171 The density of ice (kg/m^3) is represented as a Taylor series expansion in both temperature and
172 pressure:

$$173 \rho_i = [a + (b + c\Delta T) \times \Delta T] \times (1 + \alpha\Delta p) \quad (1)$$

174 and the density of liquid water (kg/m^3) is represented as:

$$175 \rho_l = [a + (b + (c + d\Delta T) \times \Delta T) \times \Delta T] \times (1 + \alpha\Delta p) \quad (2)$$

176 where $\Delta T = T - 273.15$, $\Delta p = p_l - 1\text{e}5$, T and p_l are temperature (K) and liquid pressure (>101325
177 Pa), respectively; and a , b , c , d , α are constant coefficients, listed in Table 1. Under conditions of
178 equal density, we assume $\rho_i = \rho_l$.

179

Table 1 Coefficients in density of ice and liquid

	a	b	c	d	α
ρ_i	916.724	-0.147143	-2.38e-4	–	1.0e-10
ρ_l	999.915	0.0416516	-1.01e-2	2.06e-4	5.0e-10



180 2.2 Cryosuction

181 Painter and Karra (2014) proposed a constitutive relationship for phase partitioning of water in
 182 frozen soils based on Clapeyron equation and Van Genuchten model (Van Genuchten, 1980):

$$183 \quad s_i = \begin{cases} S_*(-\beta\rho_l L_f \vartheta), \vartheta < \vartheta_f \\ S_*(p_g - p_l), \vartheta \geq \vartheta_f \end{cases}, \quad \vartheta = \frac{T(K)-273.15}{273.15}, \quad \vartheta_f = -\frac{\psi_*(1-s_g)}{\beta L_f \rho_l} \quad (3)$$

$$s_i = 1 - s_l / S_*(p_g - p_l)$$

184 where s_n is the saturation of n -phase and the subscripts $n = l, i, g$ are liquid, ice, and gas phases,
 185 respectively; β is a coefficient; L_f is the heat fusion of ice; p_n ($n = l, g$) is the pressure of n -phase;
 186 S_* is the Van Genuchten model. This physically derived formulation can describe the change of
 187 matric suction in the frozen zone due to the change of ice content, and thus has the capacity to
 188 represent cryosuction.

189 Alternatively, to exclude the effect of cryosuction in this study, we used the Van Genuchten model
 190 to determine the total water content, including liquid water and ice. The liquid water content is
 191 achieved by an empirical relationship (soil-freezing characteristic curve) which describes that the
 192 liquid water content only relates to temperature through an exponent function (McKenzie et al.,
 193 2007).

$$194 \quad s_l = s_r + (s_{\text{sat}} - s_r) \exp \left[- \left(\frac{T(K) - 273.15}{\omega} \right)^2 \right] \quad (4)$$

$$s_i = S_*(p_g - p_l) - s_l$$

195 where s_r, s_{sat} are saturations of liquid water at residual and saturated conditions, respectively; ω is
 196 a constant coefficient.

197 2.3 Advective heat transport

198 The energy conservation equation of the subsurface system is given by:

$$199 \quad \frac{\partial}{\partial t} [\phi \sum_{n=l,i,g} (\rho_n s_n u_n) + (1 - \phi) c_{v,\text{soil}} T] + \underbrace{\nabla \cdot (\rho_l h_l \mathbf{V}_l)}_{\text{advective heat}} - \underbrace{\nabla \cdot (\kappa_e \nabla T)}_{\text{conductive heat}} = Q_E \quad (5)$$

200 where ϕ is porosity; u_n is the specific internal energy of phase ($n \in \{l, i, g\}$); $c_{v,\text{soil}}$ ($\text{J m}^{-3} \text{K}^{-1}$) is
 201 the volumetric heat capacity of the soil grains. The second and third terms represent the advective
 202 and conductive heat transport in subsurface, in which h_l (J/mol) is the specific enthalpy of liquid;
 203 \mathbf{V}_l (m/s) is the velocity vector of liquid water determined by Darcy's law; and κ_e ($\text{W m}^{-1} \text{K}^{-1}$) is
 204 the effective thermal conductivity of the bulk material including soil, air, liquid water, and ice. Q_E
 205 is the sum of all thermal energy sources (W/m^3).

206 Similarly, the energy balance equation of the surface system is:



$$207 \quad \frac{\partial}{\partial t} \{[\chi \rho_l u_i + (1-\chi) \rho_i u_i] \delta_w\} + \underbrace{\nabla \cdot (h_i \chi \rho_l \delta_w \mathbf{U}_w)}_{\text{advective heat}} - \underbrace{\nabla \cdot \{[\chi \kappa_i + (1-\chi) \kappa_i] \delta_w \nabla T\}}_{\text{conductive heat}} = Q_{\text{net}} \quad (6)$$

208 in which χ is the unfrozen fraction determined by surface temperature; δ_w is ponded depth (m);
209 \mathbf{U}_w (m/s) is the velocity vector of liquid water on the surface determined by the diffusion-wave
210 approximated St. Venant equations (Gottardi and Venutelli, 1993) and Manning equation
211 (Wasantha Lal, 1998); κ_n ($\text{W m}^{-1} \text{K}^{-1}$) is the thermal conductivity of n -phase ($n = 1, i$); Q_{net} (W/m^2)
212 is the net thermal energy into and out of surface, including that from solar radiation, rain and snow
213 melt, water loss by evaporation and to the subsurface, and conductive and advected heat transport
214 to/from the subsurface. The second and third terms represent the (lateral) advective and conductive
215 heat transport that occur across the land surface.

216 3 Methods

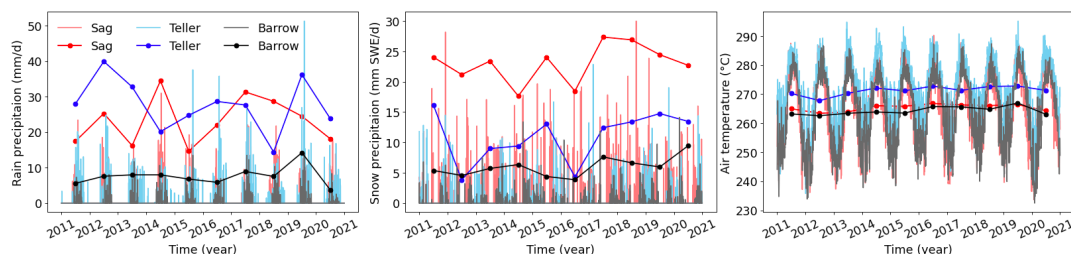
217 To evaluate the impact of representation of ice density, cryosuction, and advective heat transport
218 in permafrost modeling under different climate conditions and soil properties, we selected three
219 sites for their variance in climactic condition: Utqiagvik (Barrow Environmental Observatory,
220 71.3225°N , 156.6231°W), the headwaters of the Sagavanirktok (Sag) River (68.251°N , 149.092°
221 W), and the Teller Road Mile Marker 27 site on the Seward Peninsula (64.73°N , 165.95°W) in
222 Alaska. The simulated hydrological outputs for each site are compared in both column and
223 hillslope scenarios. Column scenarios represent expansive flat regions typical of the Arctic coastal
224 plains dominated by vertical infiltration and heat transport, and hillslope scenarios are
225 representative of the headwater, hilly terrain typical of the more inland permafrost.

226 In hillslope scenarios, hillslopes with northern and southern aspects are considered to investigate
227 physics representation comparisons under the same climate and soil condition (i.e., at a given site)
228 but different solar radiation incidence. Furthermore, hillslopes with both convergent and divergent
229 geometries are included to compare the sensitivity of simulated discharge on process
230 representation. These scenarios can incorporate many types of Arctic systems at the described plot-
231 to-regional scales, but explicitly ignore the effects of microtopography or other local-scale
232 focusing mechanisms such as water tracts or thermo-erosion gullies. The objective is to reach a
233 conclusion on the influence of the three physics representation that can be widely applicable in
234 many Arctic systems.

235 3.1 Field data description



236 For each site, data used in each simulation comprises meteorological forcing datasets for the period
237 2011-2020, averaged wind speed, and soil properties.
238 Meteorological forcing datasets are taken from the Daymet version 4 dataset (Thornton et al., 2020),
239 which provides observation-based, daily averaged weather variables through statistical modeling
240 techniques at 1 km spatial resolution (Thornton et al., 2021). Variables that are used in simulations
241 include daily average air temperature (calculated as the mean of Daymet's daily minimum and
242 maximum values), relative humidity (calculated from air temperature and Daymet's vapor
243 pressure), incoming shortwave radiation (W/m^2) (calculated as a product of Daymet's daylight
244 incoming radiation and daylength), and total precipitation (m/s), which is split into snow and rain
245 based upon the air temperature. Figure 1 illustrates the precipitation of rain, snow, and air
246 temperature in the three sites from 2011 to 2020, where the points represent the corresponding
247 averaged values per year. In terms of the forcing conditions, the annual rainfall of the Sag and
248 Teller sites range between 20 and 40 mm/d over the ten years, more than twice the rainfall typical
249 of the Barrow site. In addition, Sag has a significantly larger amount of snow every year that is
250 over double of that at the Teller site and almost five times larger compared to the Barrow site. For
251 the air temperature, Sag and Barrow are similar and colder than Teller by 7-8 degrees. In general,
252 the Barrow site is dry and cold, the Sag site is wet and cold, and the Teller site is wet and warm.



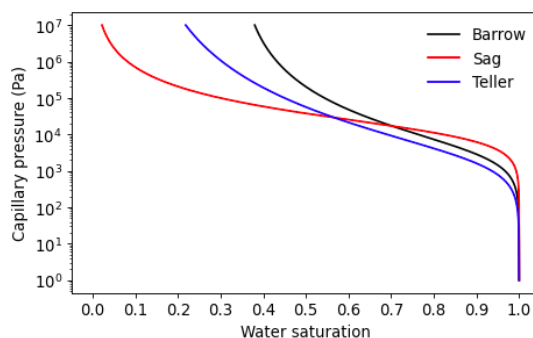
253
254 **Figure 1** Precipitation and air temperature of site Barrow, Sag, and Teller from year 2011 to 2020

255 In addition to the time series of forcing data from Daymet, we used an average wind speed for
256 each site. For Barrow and Teller, the average wind speed was estimated from the measurement
257 taken by the Next-Generation Ecosystem Experiments (NGEE) Arctic project. At Barrow, the
258 measurement was taken at area A ($71.2815^\circ N$, $156.6108^\circ W$) at the height of 1.3 meters above
259 surface (Hinzman et al., 2014). At Teller, the measurement at 3.8 m above the surface of a lower
260 level of the watershed (Busey et al., 2017) was used. For Sag, the average wind speed was
261 estimated based on the measurement at the Toolik Lake field site (near to Sag River) at the height



262 of 3.1 m above surface, which is accessible through the National Ecological Observatory Network
263 (NEON, 2021).

264 The soil properties of Barrow, Sag, and Teller, including porosity, permeability, Van Genuchten
265 parameters, and thermal conductivity parameters, were chosen from previous modeling studies at
266 these sites (Atchley et al., 2015; Jafarov et al., 2018; O'Connor et al., 2020), see (Table 2). Roughly,
267 the soil profile of each site is composed of two materials: the top organic-rich layer comprising
268 mosses, peats, and other organic rich soils measuring approximately 10-30 cm thick, and the
269 principal mineral soil. There is minor difference in thermal conductivity parameters among the
270 three sites, and soil permeability is also at the same order of magnitude. The soil-water
271 characteristic curve (SWCC) of the principal mineral soil of Barrow, Sag, and Teller, shown in
272 Figure 2, indicates that the soil property between Barrow and Teller is relatively similar, while Sag
273 differs from the other two with a relatively flat SWCC.



274
275 **Figure 2 Soil-water characteristic curve (SWCC) of soil in Barrow, Sag, and Teller**

276 Usually, at the hillslope scale, the thickness of organic layers of a watershed varies from the toe-
277 slope, through a steeper mid-hill, up to the flat top. Typically, thicker organic layers may exist at
278 the top and bottom compared to the mid-hillslope. The low thermal conductivity of organic layers
279 can impede the heat transport between the air and the underlying mineral soil, resulting in varying
280 thaw depth (or permafrost table depth) along a hillslope, which has been observed at the site Teller
281 (Jafarov et al., 2018). In this paper, hillslope meshes were constructed following this observation
282 so that the organic layers are thicker at the top and bottom of a hillslope, as described in the next
283 section.

284 **3.2 Mesh design and material properties**

285 The comparison of different physics representations was conducted in both column and hillslope



286 scenarios.

287 The column model was designed as a one-dimensional, 50 m deep domain. The column domain
 288 was discretized into 78 cells with gradually increasing cell thickness, starting from 2 cm at the soil
 289 surface to 2 m at the bottom of the domain. We assigned different material properties to the cells
 290 to represent different soil layers. A column domain is divided into three layers, and the thickness
 291 of each layer was designed differently among the three sites according to geological observations
 292 (Jan et al., 2020; O'Connor et al., 2020; NGEE-Arctic). Specifically, from top to bottom, the three
 293 layers of the Barrow soil column are 2 cm-thick moss, 8 cm-thick peat, and mineral; for Teller, the
 294 soil column consists of a 4 cm moss layer, a 22 cm peat layer, and mineral; and the three layers of
 295 the Sag soil column are acrotelm, catotelm, with thickness of 10 cm and 14 cm, respectively, and
 296 the remainder mineral. The soil properties of each layer at three sites are listed in Table 2.

297 **Table 2 Soil properties of three soil layers of all sites used in this paper**

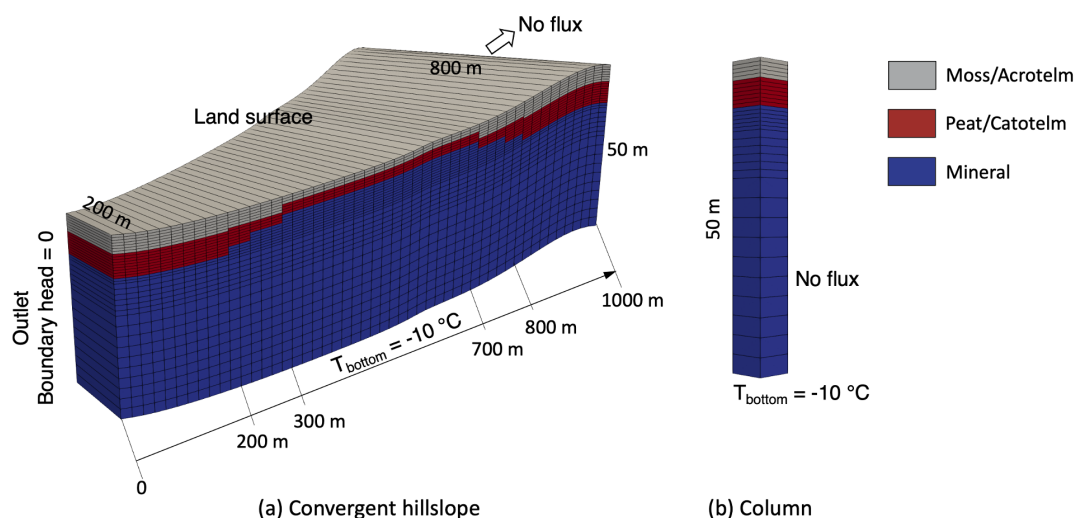
Site	Barrow			Sag			Teller		
Layers	moss	peat	mineral	acrotelm	catotelm	mineral	moss	peat	mineral
Porosity	0.9	0.876	0.596	0.878	0.796	0.457	0.9	0.55	0.45
Permeability (m ²)	1.7e-11	9.38e-12	6e-13	2.64e-10	9.63e-12	3.98e-13	5e-11	5e-12	2e-13
VG α (Pa ⁻¹)	2.3e-3	9.5e-4	3.3e-4	7.93e-4	1.75e-4	8.06e-5	2.35e-3	2.93e-4	5.45e-4
VG n	1.38	1.44	1.33	1.405	1.566	1.571	1.38	1.269	1.236
Residual saturation	0.056	0.388	0.334	0.0073	0.0662	0.	0.1	0.	0.1
Thermal conductivity, unfrozen (Wm ⁻¹ K ⁻¹)	0.446	0.427	0.788	0.519	0.630	1.309	0.57	0.67	1
Thermal conductivity, dry (Wm ⁻¹ K ⁻¹)	0.024	0.025	0.104	0.066	0.086	0.265	0.07	0.07	0.29

298

299 In the hillslope scenario, we designed the mesh based on observations at Teller to represent a
 300 generalized, varying-thickness low Arctic hillslope. A hillslope mesh was created first by
 301 generating a pseudo-2D surface mesh with 50 cells and then extruding the 2D mesh downward by
 302 50 m. The pseudo-2D surface was designed in a trapezoidal shape with a single, variable-width
 303 cell in the cross-slope direction to represent convergent/divergent hillslopes, the short and long
 304 sides of which are 200 m and 800 m, respectively (see Figure 3). Vertically, from surface
 305 downward, the grid size distribution was the same as the column mesh for each site. The domain
 306 is also composed of three layers, same as the column, while the numbers of cells representing each
 307 soil layer (i.e., soil layer thickness) are different along the hillslope. The thickness distribution of
 308 the first two layers of each site is shown in Table 3. The third layer of a hillslope for all sites is the
 309 principal mineral soil. Additionally, hillslope meshes with different aspects (i.e., north, south) were



310 also created.



311 (a) Convergent hillslope (b) Column
 312 **Figure 3 Schematic domain mesh and soil layer partition: (a) example of a convergent hillslope domain, (b)**
 313 **column domain.**

314 **Table 3 Thickness distribution of the organic layers along hillslope for each site**

Site	Horizontal x range (m)	Barrow layer thickness (cm)	Sag layer thickness (cm)	Teller layer thickness (cm)
Layer 1 Moss/Acrotelm	0 ~ 200	2	14	8
	300 ~ 700	2	6	4
	800 ~ 1000	2	14	8
Layer 2 Peat/Catotelm	0 ~ 200	12	18	22
	300 ~ 700	6	8	22
	800 ~ 1000	12	18	22

315 3.3 Model setup

316 To study how the representations of the three physical processes (i.e., ice density, cryosuction, and
 317 advective heat transport) affect simulated hydrological outputs at different scales and hillslope
 318 topography features, and under various forcing and soil conditions, 62 model simulations were
 319 conducted, summarized in Table 4. To examine the validity of the assumption of equal density
 320 between ice and liquid, we included cryosuction and advective heat transport in models. To
 321 investigate the role of cryosuction in permafrost modeling, we used different density, while
 322 neglecting advective heat transport to decrease the computation cost. Note that neglecting
 323 advective heat transport in these runs can reduce the effect of cryosuction on simulation predictions,
 324 as cryosuction moves water which would itself advect energy. To compare the difference between
 325 neglecting and including heat advection, we used different density expressions for ice and liquid,



326 and included cryosuction. Particularly, in order to understand the impact of advective heat
 327 transport on permafrost process when soil is at its wettest, we designed two extreme cases under
 328 the warm, wet conditions of the Teller site in which soil evaporation was artificially reduced.
 329 These runs were designed to maximize water flux and therefore maximize the potential for
 330 advective heat transport to affect predictions.

331 **Table 4 Ensemble of models designed in this study**

To compare	Site	Scale	Geometry	Aspect	Remark
• $\rho_i \neq \rho_1$, Eq. (1)	Barrow	column	–	–	• heat advection
		hillslope	convergent	north	
• $\rho_i = \rho_1$, Eq. (2)	Sag	hillslope	divergent	north	• cryosuction
				south	
• Include heat transport	Barrow	column	–	–	• $\rho_i \neq \rho_1$
		hillslope	convergent	north	
• Neglect heat transport	Sag	hillslope	divergent	north	• cryosuction
				south	
	Extreme case, Teller	hillslope	convergent	north	• reduced evaporation
• Include cryosuction	Barrow	column	–	–	• $\rho_i \neq \rho_1$
		hillslope	convergent	north	
• Neglect cryosuction	Sag	hillslope	divergent	north	• no heat advection
				south	

332
 333 Prior to simulating all cases, two steps of initialization are carried out for each site. First, a column
 334 model with a given initial water table depth and above-0 °C temperature was frozen by setting the
 335 bottom temperature at a constant value of -10 °C until a steady-state frozen soil column is formed.
 336 The initial water table depth is chosen to ensure that the frozen column’s water table, after
 337 accounting for expansion of ice, is just below the soil surface. The pressure and temperature
 338 profiles of the frozen column were used as the initial conditions of the second step initialization.
 339 Before proceeding, the observed forcing data (period of 2011-2020) was averaged across the years
 340 to form a one-year, “typical” forcing year, which was then repeated 10 times. Using this typical
 341 forcing data and the solutions of the first step, we solved the column model in a transient solution,
 342 calculating an annual cyclic steady-state and obtaining the pressure and temperature fields at the
 343 end of the 10th year. The final state was then used as initial condition in formal simulations listed
 344 in Table 4. The temperature at bottom was constant at -10 °C.

345 **3.4 Evaluation metrics**



346 To fully assess the effect of representation of ice density, advective heat transport, and cryosuction
347 in permafrost hydrology modeling, we used root mean squared error (RMSE) and normalized
348 Nash–Sutcliffe efficiency (NNSE) as performance metrics. RMSE has the same dimension with
349 the corresponding variables, which can be used to evaluate the average absolute deviation from a
350 benchmark, defined by:

$$351 \text{ RMSE} = \sqrt{\frac{\sum_{t=1}^N (x_t - y_t)^2}{N}} \quad (7)$$

352 where x_t and y_t are the two modeled datasets to compare from the initial time point ($t = 1$) to the
353 end ($t = N$).

354 NNSE is a normalized dimensionless metric describing the relative relationship between an
355 estimation and a reference, which is oftentimes used for evaluating hydrological models.

$$356 \text{ NNSE} = 1 / \left(1 + \frac{\sum_{t=1}^N (x_t - y_t)^2}{\sum_{t=1}^N (x_t - \bar{x})^2} \right) \quad (8)$$

357 where the modeled results x_t (obtained without physics simplification) is considered as the
358 benchmark, and \bar{x} is the mean value of the benchmark. NNSE approaching to 1 indicates perfect
359 correspondence between two observations.

360 In addition, we also used normalized mean absolute error (MAE) to quantify the percentage change
361 of results obtained with simplified physics relative to full physical representations (see Section
362 4.4).

$$363 \text{ Normalized MAE} = \frac{\sqrt{\sum_{t=1}^N |x_t - y_t| / N}}{\text{normalizing reference}} \times 100\% \quad (9)$$

364 Two normalizing references were selected considering different model output variables. For
365 instance, in terms of temperature and saturation which fluctuate between two non-zero values, the
366 annually averaged variation range was chosen as the reference.

$$367 \text{ Normalizing reference} = \frac{\sum_{\text{year}=1}^{\text{num of years}} (\text{maximum} - \text{minimum})}{\text{number of years}}$$

368 For variables with zero as the smallest value, such as evaporation, discharge, and thaw depth, the
369 corresponding average value was selected as the reference.

370 4 Results

371 This section compares simulated outputs over the period of 2011-2020 for the three physics under
372 different simulating conditions. We focus on the impact on integrated variables, such as
373 evaporation, discharge, averaged thaw depth, and depth-dependent variables, such as temperature,

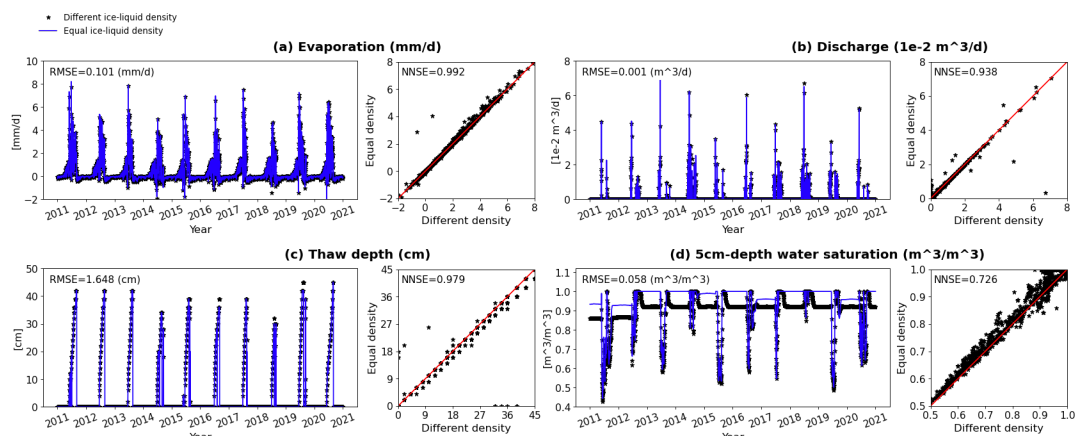


374 and total water saturation (ice and liquid). For hillslope models, we chose five surface locations
375 according to the slope geometry to collect simulated data, which were then averaged to obtain a
376 single outcome for each variable of interest.

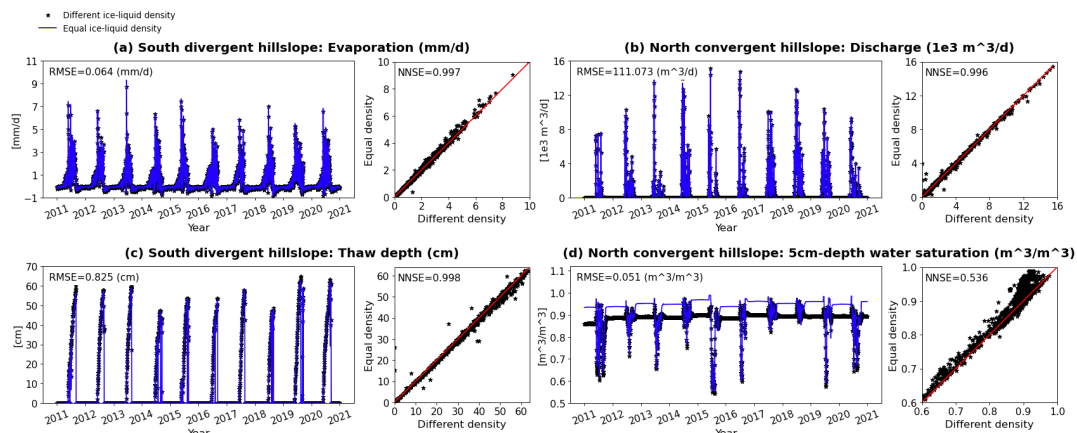
377 **4.1 Ice density**

378 To evaluate the representation of ice density on permafrost process simulation, we compared
379 evaporation, discharge, thaw depth, and total water saturation between simulations using equal and
380 different ice density expressions. Figure 4 and Figure 5 show an example of the comparison under
381 conditions of Sag at column and hillslope scale, respectively. Results are compared in both time
382 series and correlation.

383 Generally, at both column and hillslope scale, assuming equal density between ice and liquid has
384 minor impacts on evaporation, discharge, and thaw depth over the 10-year simulation, except at a
385 few deviated points as shown in the correlation figures. According to column-based models, the
386 RMSEs of evaporation, discharge, and thaw depth are 0.101 mm/d, 0.001 m³/d, and 1.648 cm,
387 respectively, one order of magnitude smaller than the corresponding variable values. At hillslope
388 scale, see Figure 5, the south-facing divergent hillslope is selected to show modeling comparison
389 on evaporation and thaw depth, in that they are potentially mostly affected when a hillslope has a
390 south orientation and divergent geometry. Likewise, the north-facing convergent hillslope is
391 chosen to compare discharge and water saturation from simulations with different density
392 expression. Even then, RMSEs of the three variables are 0.064 mm/d, 111.073 m³/d, and 0.825 cm,
393 respectively, two orders of magnitude smaller than the corresponding variable values at hillslope
394 scale. Besides, NNSEs of the three variables output from both column and hillslope simulation are
395 over 0.9, approaching 1 especially at the hillslope scale. Therefore, all indicate good performance
396 of equal ice-liquid density assumption in predicting integrated variables and thaw depth. By
397 comparison, the estimation of water saturation is relatively affected by the density assumption
398 during cold seasons within a year, as shown by Figure 4 (d) and Figure 5 (d). This is reasonable in
399 that when water mainly exists in the form of ice, equal ice-liquid density assumption will
400 overestimate the water content.



401
402 **Figure 4 Comparison of column simulations between different and equal ice-liquid density under conditions**
403 **of Sag, in (a) evaporation, (b) discharge, (c) thaw depth, and (d) water saturation at 5 cm beneath surface**
404 **from year 2011 to 2020.**

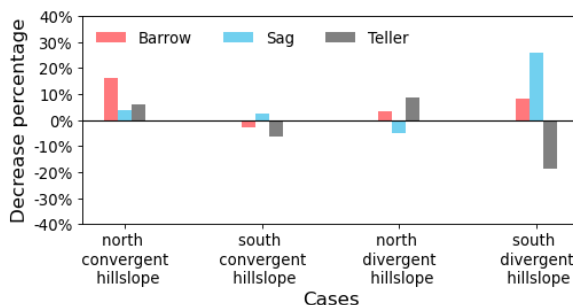


405
406 **Figure 5 Comparison of hillslope simulations between using different and equal ice-liquid density under**
407 **conditions of Sag, in (a) evaporation, (b) discharge, (c) thaw depth, and (d) water saturation at 5 cm beneath**
408 **surface from year 2011 to 2020.**

409 In addition, we investigated how much the assumption of equal ice-liquid density can affect
410 simulation time at hillslope scale. Using 10-year simulations with real ice density as references,
411 the percentage change of time consumed after applying equal ice-liquid density was calculated and
412 displayed in Figure 6. Overall, under the density assumption, it may take less time (positive
413 percentage), but no more than 25% and on average lower than 10%. However, it may also increase
414 computational time (negative percentage) mainly under wet conditions, such as at Sag and Teller.
415 Thus, given a long-period large-scale modeling of permafrost freezing and thaw process, there is
416 no consistent conclusion on whether equal ice-liquid density can ease computational cost. It



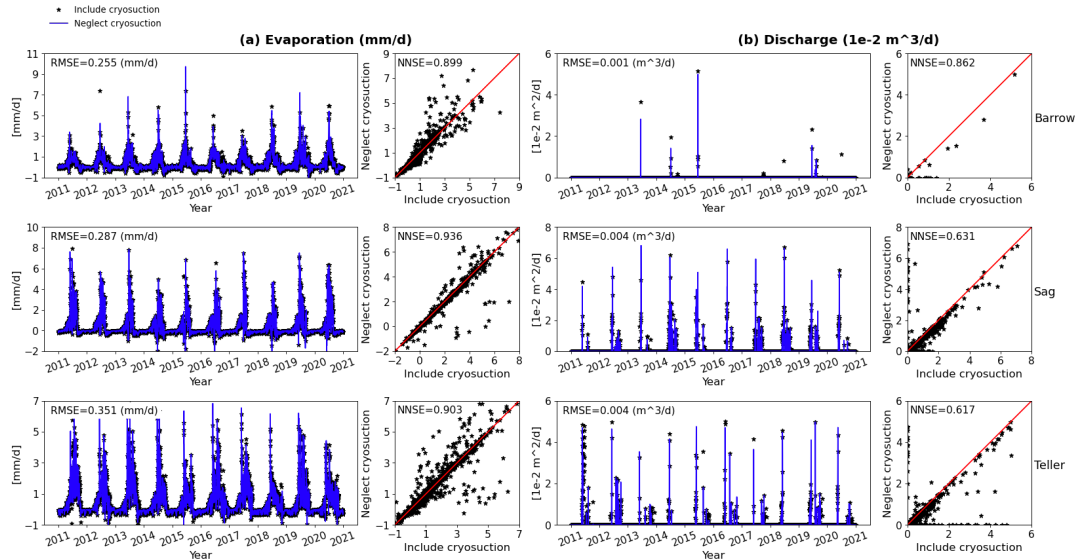
417 depends on both the weather conditions and soil properties.



418
419 **Figure 6 Decreased percentage of simulation time under the assumption of equal ice-liquid density compared**
420 **to the real ice density representation for all hillslope scale simulations.**

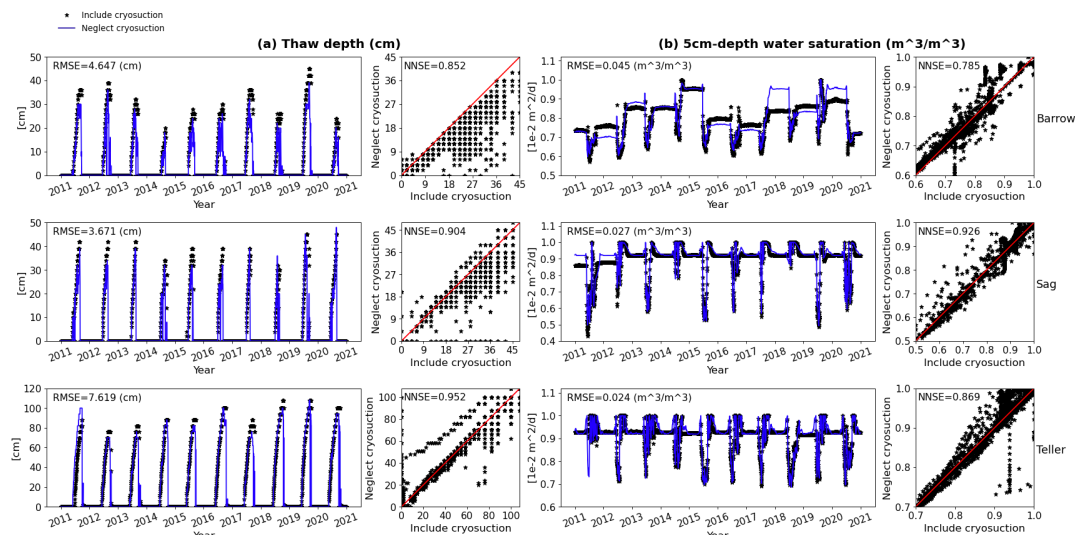
421 4.2 Cryosuction

422 To evaluate the effect of cryosuction on permafrost process predictions, we compared evaporation,
423 discharge, thaw depth, total water saturation, and temperature obtained through simulations
424 including and neglecting cryosuction. Figure 7 through Figure 9 illustrate column-scale
425 comparisons of these variables under conditions at three sites (Barrow, Sag, and Teller). Figure 7
426 presents the effect of excluding cryosuction on evaporation and discharge. RMSE of evaporation
427 from the three sites ranges between 0.25 mm/d and 0.35 mm/d, still one order of magnitude smaller
428 than the common evaporation rate. Evaporation NNSEs of the three sites are around 0.9. For
429 discharge, RMSEs are also one order of magnitude smaller than the average, whereas NNSEs fall
430 between 0.6 and 0.9. Generally, cryosuction plays a more important role in predicting discharge
431 compared to evaporation, especially under warm and wet climate conditions, such as Teller.



432
 433 **Figure 7 Comparison of column simulations between including and neglecting cryosuction under conditions**
 434 **of Barrow, Sag, and Teller, in (a) evaporation, (b) discharge.**

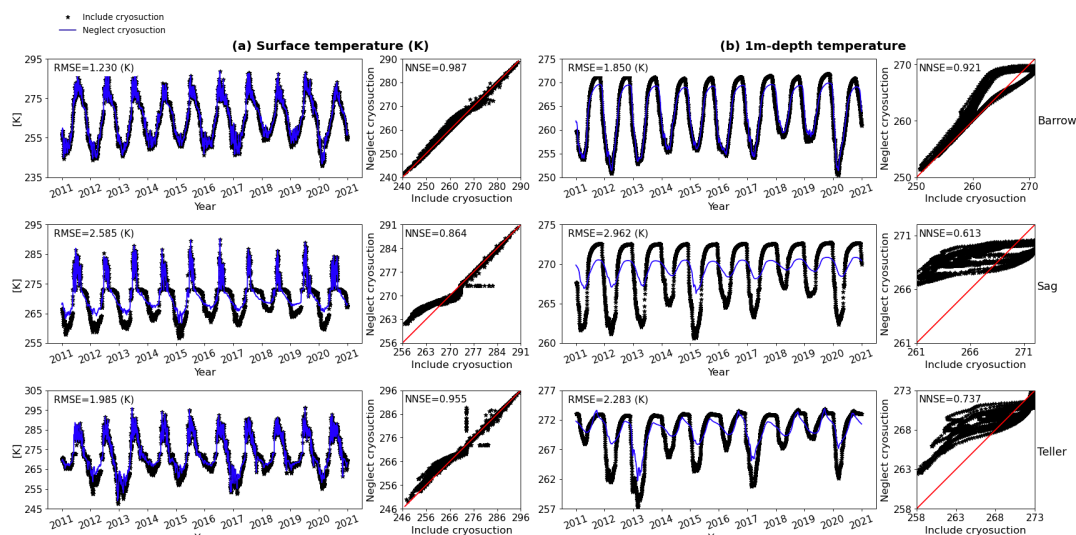
435 Figure 8 shows the effect of cryosuction on column-scale simulated thaw depth and total water
 436 saturation at 5 cm beneath surface. RMSEs of thaw depth range from 3 cm to 8 cm. Though still
 437 one order of magnitude smaller than the average annual thaw depth, the estimation error due to
 438 neglecting cryosuction is obvious in summer, especially at areas with cold temperature and low
 439 rainfall like Barrow. By comparison, at Teller, where the largest thaw depth is over double of
 440 Barrow and Sag due to its higher temperature, soil cryosuction does not essentially affect thaw
 441 depth compared to the other two sites. Similarly, for the total water saturation, at Barrow, the effect
 442 of cryosuction is more clearly observed, not only during cold seasons as observed for density
 443 representation (section 4.1), but also in summers.



444
 445 **Figure 8 Comparison of column simulations between including and neglecting cryosuction under conditions**
 446 **of Barrow, Sag, and Teller, in (a) thaw depth, (b) water saturation at 5 cm beneath surface.**

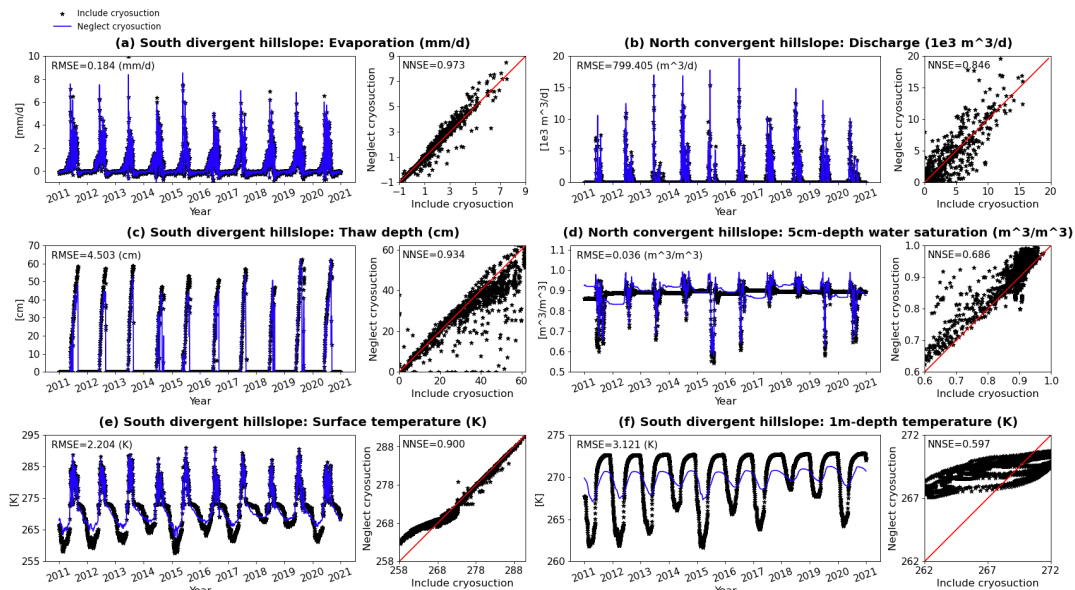
447 Finally, we also compared soil temperature obtained from models with or without cryosuction
 448 included; see Figure 9. Surface temperature is little affected by cryosuction, except at the Sag site,
 449 where the surface temperature is overestimated during winter. At 1 m depth, soil temperature of
 450 Barrow is slightly changed in summer due to neglecting cryosuction. At both Sag and Teller, the
 451 fluctuation range of temperature at 1 m beneath land surface is underestimated if cryosuction effect
 452 is not considered, especially at Sag, NNSE decreases to 0.6 approximately.

453 Therefore, from Figure 7 to Figure 9, neglecting cryosuction effect at column scale simulation has
 454 less impact on integrated hydrological variables, but will cause significant difference when
 455 estimating thaw depth and location-based variables. The difference among variables varies under
 456 different climate conditions. Influence on integrated variables, such as evaporation and discharge,
 457 are more obviously under warm and wet conditions (Teller); thaw depth and water saturation are
 458 affected more under cold and low-rainfall conditions (Barrow); and soil temperature tends to be
 459 influenced greater under cold and high precipitation (rain and snow) conditions (Sag).



460
 461 **Figure 9 Comparison of column simulations between including and neglecting cryosuction under conditions**
 462 **of Barrow, Sag, and Teller, in (a) surface temperature, (b) temperature at 1 m beneath surface.**

463 Neglecting soil cryosuction has a similar impact on hydrological outputs in hillslope scale models.
 464 Figure 10 shows the comparison of the variables discussed above under the Sag climate.
 465 Evaporation, thaw depth, and temperature are presented based on south-facing divergent hillslope
 466 models, while discharge and water saturation are from hillslope models with north-facing
 467 convergent geometry. In general, neglecting soil cryosuction has a smaller effect on integrated
 468 variables (evaporation and discharge) compared with other pointwise variables. Though thaw
 469 depth presents a high NNSE, approximately 0.94, and low RMSE, about 4.5 cm compared to the
 470 average, indicating a good match between models considered and excluded cryosuction, the
 471 estimation error during summer may reach as high as 10 cm, particularly from 2011 to 2017, as
 472 shown in Figure 10 (c). Obvious errors in water saturation and temperature, similar with column-
 473 scale models, occur almost annually with respect to extrema during winter and summer. Overall,
 474 compared to column-scale models, differences in evaporation, discharge, thaw depth, and surface
 475 temperature due to neglecting cryosuction effect are relatively reduced at hillslope scale if
 476 comparing NNSEs (Table 5). Localized subsurface variables, such as water saturation and 1m-
 477 depth soil temperature, show increased errors from column to hillslope scale models, which is
 478 primarily caused by lateral flux exchange captured by hillslope modeling.



479
 480 **Figure 10** Comparison of hillslope simulations between including and neglecting cryosuction under conditions
 481 of Sag, in (a) evaporation, (b) discharge, (c) thaw depth, (d) water saturation at 5 cm beneath surface, (e)
 482 surface temperature, (f) temperature at 1 m beneath surface.

483 **Table 5** NNSE of outputs from column and hillslope models under conditions of Sag
 484 shown in Figure 7 through Figure 10

Scale	Evaporation (mm/d)	Discharge (m ³ /d)	Thaw depth (cm)	5cm-depth water saturation (-)	Surface temperature (K)	1m-depth temperature (K)
Column	0.936	0.631	0.904	0.926	0.864	0.613
Hillslope	0.973	0.846	0.934	0.686	0.900	0.597

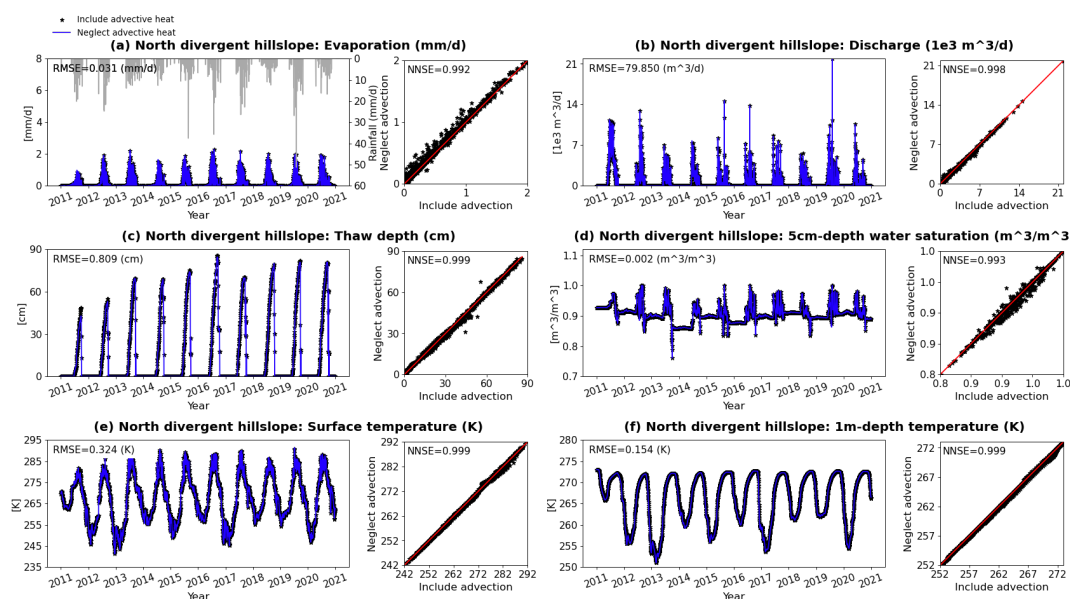
485

486 4.3 Advective heat transport

487 This section evaluates the performance of advective heat transport in modeling permafrost process.
 488 As above, we investigated the influence of neglecting heat advection on evaporation, discharge,
 489 thaw depth, total water saturation, and temperature. Overall, heat advection does not play a vital
 490 role in a normal Arctic system after comparing all hydrological outputs from models with different
 491 heat transport representations. Comparisons based on column-scale and hillslope-scale models are
 492 not shown here (see Supplement); instead, the extreme case under conditions of Teller is presented
 493 (Figure 11). Teller is abundant in rainfall over the period of 2011-2020 (Figure 1). In the extreme
 494 case, evaporation was reduced factitiously to almost a quarter of the original value (see Figure 7
 495 (a) at Teller and Figure 11 (a)) for the purpose of increasing water flow rates. For instance,
 496 discharge has quadrupled after adjusting evaporation by comparing Figure 11 (b) and Figure 7 (b)



497 at Teller. This specific scenario is chosen to maximize the potential effect of advective heat
 498 transport in a hillslope-scale Arctic system. Figure 11 illustrates comparisons on all outputs
 499 mentioned above from hillslope models without heat advection and with full thermal
 500 representation. Apparently, all RMSEs are extremely small, at least two orders of magnitude lower
 501 than the corresponding variable average. Almost all NNSEs are approximately one, even for thaw
 502 depth, localized water saturation, and temperature. Therefore, for most Arctic systems at this scale,
 503 it is reasonable to neglect advective heat transport.

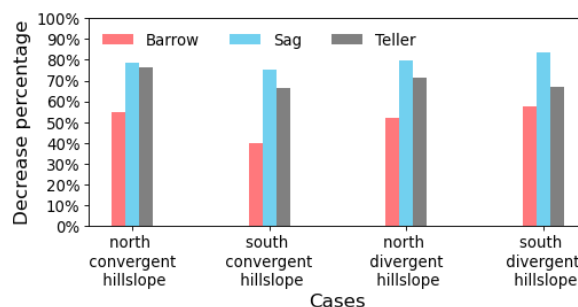


504
 505 **Figure 11 Comparison of hillslope simulations between including and neglecting advective heat transport**
 506 **under extreme conditions of Teller, in (a) evaporation, (b) discharge, (c) thaw depth, (d) water saturation at 5**
 507 **cm beneath surface, (e) surface temperature, (f) temperature at 1 m beneath surface.**

508 In addition to simulated results, we also compared simulation times in percentage change between
 509 hillslope models neglecting and including heat advection. ATS uses Algebraic Multigrid method
 510 as preconditioner for solving, which has a relatively deficient performance in dealing with
 511 hyperbolic equations. Thus, incorporating advective heat transport will aggravate computational
 512 cost, particularly in case of both large spatial and temporal scale. Figure 12 shows the relative
 513 percentage reduction in computational time for 10-year simulations after excluding heat advection
 514 in both surface and subsurface thermal flux. It drops by 70% ~ 80% under wet conditions (e.g.,
 515 Sag and Teller) and 40% ~ 60% under dry conditions (e.g., Barrow). Hence, neglecting advective
 516 heat transport considerably improves the performance of large spatial-temporal permafrost



517 hydrology simulations.



518
 519 **Figure 12** Decreased percentage of simulation time after neglecting heat advection compared to full thermal
 520 representation for all hillslope scale simulations.

521 4.4 Comprehensive comparison

522 In the above three sections, we discussed time-series simulation comparisons. This section will
 523 analyze the effect of equal ice-liquid density, neglecting cryosuction, and neglecting heat
 524 advection on permafrost modeling outputs from holistic, average perspectives.

525 First, we extracted NNSEs of all variables obtained from all comparing models for qualitative
 526 analysis. Table 6 shows an example based on column-scale models under conditions of three
 527 different sites. Red numbers highlight the obviously reduced NNSEs of one or two processes
 528 among the three for each variable. Overall, neglecting advective heat transport has the least
 529 influence on model outputs. Equal ice-liquid density primarily affects saturation and has less effect
 530 on other variables. Excluding soil cryosuction makes the greatest impact on almost all variables,
 531 especially in a relatively wet environment. Among the variables, evaporation and surface
 532 temperature are less affected by the three physical process representations, while location-based
 533 water saturation is most affected.

534 **Table 6** A summary of NNSEs of variables obtained through column model comparison

Variables	Barrow			Sag			Teller		
	Heat advection	Ice density	Cryosuction	Heat advection	Ice density	Cryosuction	Heat advection	Ice density	Cryosuction
Evaporation	0.9971	0.9942	0.8991	0.9926	0.9917	0.9365	0.9989	0.9958	0.9033
Discharge	0.9235	0.6282	0.8615	0.9962	0.9377	0.6305	0.9854	0.9874	0.6175
Thaw depth	0.9970	0.9961	0.8517	0.9910	0.9791	0.9036	0.9969	0.9887	0.9524
5cm-depth s_w	0.9959	0.9335	0.7851	0.9916	0.7260	0.9260	0.9979	0.5618	0.8690
40cm-depth s_w	0.9932	0.0221	0.2130	0.9951	0.0622	0.3111	0.9990	0.2807	0.8498
Surface T	0.9999	0.9999	0.9871	0.9993	0.9990	0.8642	0.9999	0.9996	0.9554
1m-depth T	0.9999	0.9999	0.9207	0.9997	0.9996	0.6127	0.9997	0.9991	0.7366



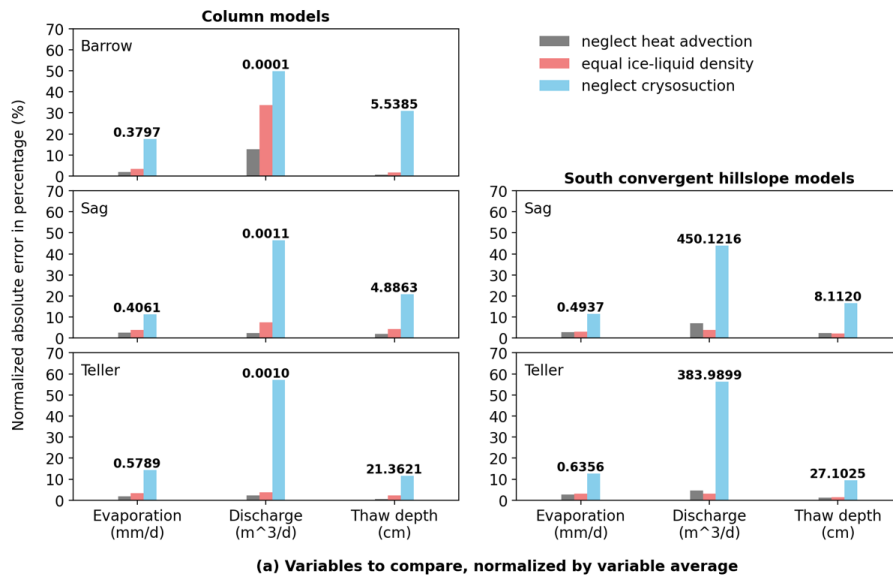
535 * s_w and T in Table 6 are water saturation and temperature, respectively.
536 Furthermore, to compare across the physics quantitatively, we calculated the mean absolute error
537 (MAE) for each variable of interest over the simulation period of 2011-2020. For evaporation,
538 discharge, and thaw depth, the MAEs are normalized by the corresponding variable average
539 (numbers in Figure 13 (a)); for water saturation and temperature, the MAEs are normalized by
540 their average annual fluctuation range (numbers in Figure 13 (b)). All normalized MAEs are
541 presented in percentage, displayed in Figure 13 according to column- and hillslope-scale (e.g.,
542 south-facing convergent hillslope) models under three different climate conditions. Hillslope-scale
543 model output under conditions of Barrow is not shown in that flat land occupies a majority of the
544 area. A larger normalized MAE percentage indicates greater impact on the variable resulted from
545 a physical process.

546 From the perspective of 10-year average, in general, each physical process of Arctic system
547 discussed in this paper presents a similar impact on variables between column and hillslope scales.
548 Under climate and soil conditions of three different sites, neglecting cryosuction in permafrost
549 modeling leads to the greatest influence on hydrological prediction amongst the three physical
550 assumptions. As seen in Figure 13 (a), it will result in 10% ~ 20% deviation in evaporation, 50%
551 ~ 60% in discharge, and 10% ~ 30% in thaw depth. Evaporation is the least affected among the
552 three variables. Discharge is more affected in regions with abundant rainfall (Teller), while in
553 regions with less precipitation, evaporation and thaw depth are relatively affected (Barrow). By
554 comparison, assuming equal ice-liquid density and neglecting advective heat transport may only
555 cause 10% and 5% or even much lower error, respectively, in reference to the annual average of a
556 variable. Specially in Barrow, models utilizing the same ice and liquid densities and ignoring
557 advective heat seem to make an obvious impact on discharge, whereas this also results from its
558 extremely low discharge (Figure 7 (b)).

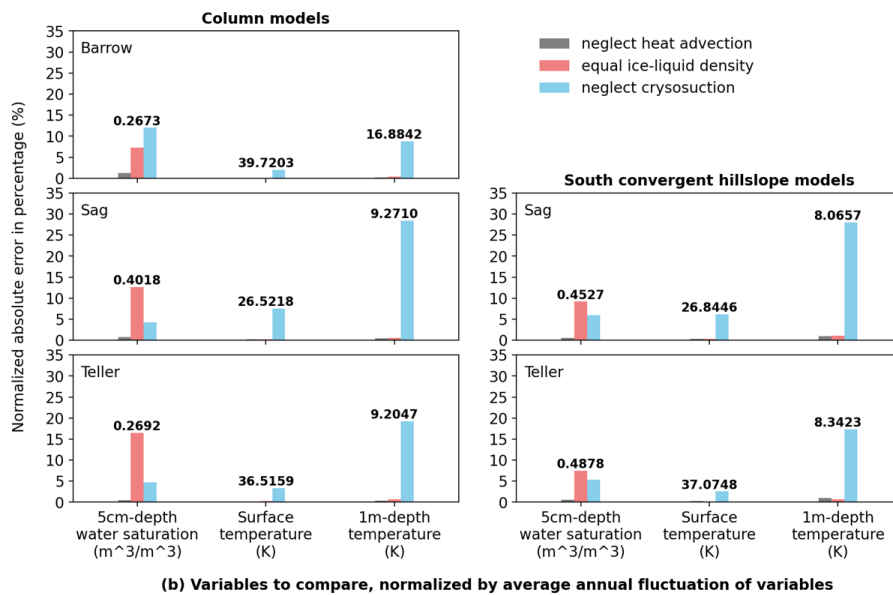
559 Figure 13 (b) illustrates the normalized MAEs of water saturation at 5 cm beneath surface, as well
560 as temperature at surface and 1 m depth. The assumption of equal ice-liquid density primarily
561 affects the estimation of water saturation profile. It can lead to about 5% ~ 15% error relative to
562 the annual change range, and the error percentage tends to slightly decrease when applying
563 hillslope-scale models due to the inclusion of lateral flow. Apart from this, neglecting soil
564 cryosuction still makes the largest impact. Surface temperature is the least affected variable among
565 all these model outputs even if cryosuction is not included in modeling. However, at 1 m depth,



566 error can increase to 10% ~ 30% by simulation without cryosuction representation.



567
568



569
570 **Figure 13** Normalized average absolute error of variables over the period of 2011-2020, compared among
571 **three physical assumptions at column and hillslope scales. Variables: (a) evaporation, discharge, and thaw**
572 **depth, numbers in figures are the average values of the corresponding variables; (b) water saturation, and**
573 **temperature, numbers in figures are the average annual fluctuation range of each variable.**

574 **5 Conclusion**



575 Simplification of Arctic process representation is an essential consideration when developing
576 process-rich models for thermal permafrost hydrology. There are three subsurface processes that
577 are commonly described in a simplified approach for many Arctic tundra models: (i) ice is
578 prescribed the same density as liquid water; (ii) the effect of soil cryosuction is neglected; (iii)
579 advective heat transport is neglected. Here we investigated the influence of these simplified
580 representations on modeling field-scale permafrost hydrology.

581 To do this, we conducted an ensemble of simulations using the Advanced Terrestrial Simulator
582 (ATS v1.2) to evaluate the impact of the above three process simplifications on field-scale
583 predictions. The ensemble of simulations consisted of 62 numerical experiments considering
584 various conditions, including different climate conditions and soil properties at three sites of
585 Alaska, and different model scale conceptualizations. For evaluation, we compared integrated
586 variables (evaporation, discharge), averaged thaw depth, and pointwise variables (temperature,
587 total water saturation), among different models to assess the deviation of applying a simplified
588 modeling assumption. The main conclusions of this study are summarized as follows:

- 589 1) Excluding soil cryosuction in permafrost models can cause significant bias in most
590 hydrological variables. Especially, according to this study, the average deviation in
591 evaporation, discharge, and thaw depth may reach 10% ~ 20%, 50% ~ 60%, and 10% ~
592 30%, respectively, relative to the corresponding annual average values. The prediction
593 error for discharge may grow if rainfall rates increase. In the case of pointwise variables,
594 the error in temperature increases from a small amount at the surface up to 10% ~ 30% at
595 1 m beneath surface. The prediction of subsurface temperature and water saturation is
596 especially affected when considering hillslope scale models. Therefore, soil cryosuction
597 should be included when modeling permafrost change.
- 598 2) Assuming equal ice-liquid density will not result in especially large deviations when
599 predicting most of the hydrological variables, particularly at hillslope scales. It primarily
600 affects the prediction of soil water saturation profile and can cause 5% ~ 15% error relative
601 to the annual saturation fluctuation range. This difference may have consequences for the
602 carbon cycle with regards to the production of methane versus carbon dioxide. Assigning
603 liquid water density for ice may reduce computational time to a small extent in ATS,
604 dependent on simulating conditions and spatial and temporal scales.
- 605 3) For a general Arctic tundra system, the prediction error in most variables after neglecting



606 advective heat transport is less than 5%, or even much lower. In the case of ATS, the
607 simulation time cost for hillslope-scale models can decrease by 40% to 80% under
608 conditions in this study. Ignoring heat advection in the absence of local, flow-focusing
609 mechanisms, such as thermo-erosion gullies, seems a reasonable decision.

610 Through the comparison of permafrost hydrological outputs obtained from ensemble model setup
611 targeted at field scale, we confirm the importance and necessity of including soil cryosuction effect
612 in predicting permafrost changes, and valid application of equal ice-liquid density and neglecting
613 advective heat transport for a general Arctic system. The latter two may also ease computational
614 cost dependent upon simulation conditions. We expect that this study can contribute to the
615 development of permafrost hydrology models, as well as better selection of physical process
616 representations for modelers.

617 **Code availability**

618 Advanced Terrestrial Simulator (ATS) is an open-source code for solving ecosystem-based,
619 integrated, distributed hydrology, and available at <https://github.com/amanzi/ats>. Simulations were
620 conducted using version 1.2 (Coon et al., 2021).

621 **Data availability**

622 Data sources of wind speed are cited in the text. The raw forcing data acquired from Daymet, the
623 processed forcing data used for simulation, and simulation output data are available through
624 https://github.com/gaobhub/data_for_paper_model_comparison.

625 **Author contributions**

626 Bo Gao did some revision of the code to add options for process representations, designed
627 numerical experiments and setup models, did data analysis and interpretation, drafted and revised
628 the article. Ethan T. Coon implemented the code in which the study was done, conceptualized the
629 study, helped debug the runs, and helped draft and revise the article.

630 **Competing interests**

631 The authors declare that they have no conflict of interest.



632 **Acknowledgement**

633 Both authors are supported by the U.S. Department of Energy, Office of Science, Biological and
634 Environmental Research program under the InterFACE project. This research used resources of
635 the Compute and Data Environment for Science (CADES) at the Oak Ridge National Laboratory,
636 which is supported by the Office of Science of the U.S. Department of Energy under Contract No.
637 DE-AC05-00OR22725.

638 **References**

- 639 Abolt, C. J., Young, M. H., Atchley, A. L., Harp, D. R., and Coon, E. T.: Feedbacks Between
640 Surface Deformation and Permafrost Degradation in Ice Wedge Polygons, Arctic Coastal Plain,
641 Alaska, *J. Geophys. Res. Earth Surf.*, 125, e2019JF005349,
642 <https://doi.org/10.1029/2019JF005349>, 2020.
- 643 Atchley, A. L., Painter, S. L., Harp, D. R., Coon, E. T., Wilson, C. J., Liljedahl, A. K., and
644 Romanovsky, V. E.: Using field observations to inform thermal hydrology models of permafrost
645 dynamics with ATS (v0.83), *Geosci. Model Dev.*, 8, 2701–2722, [https://doi.org/10.5194/gmd-8-](https://doi.org/10.5194/gmd-8-2701-2015)
646 2701-2015, 2015.
- 647 Berteaux, D., Gauthier, G., Domine, F., Ims, R. A., Lamoureux, S. F., Lévesque, E., and Yoccoz,
648 N.: Effects of changing permafrost and snow conditions on tundra wildlife: critical places and
649 times, *Arct. Sci.*, 3, 65–90, <https://doi.org/10.1139/as-2016-0023>, 2017.
- 650 Bui, M. T., Lu, J., and Nie, L.: A Review of Hydrological Models Applied in the Permafrost-
651 Dominated Arctic Region, *Geosciences*, 10, 401, <https://doi.org/10.3390/geosciences10100401>,
652 2020.
- 653 Busey, B., Bolton, B., Wilson, C., and Cohen, L.: Surface Meteorology at Teller Site Stations,
654 Seward Peninsula, Alaska, Ongoing from 2016, Next Generation Ecosystem Experiments Arctic
655 Data Collection, Oak Ridge National Laboratory, U.S. Department of Energy, Oak Ridge,
656 Tennessee, USA. Dataset accessed on October 10, 2021 at <https://doi.org/10.5440/1437633>,
657 2017.
- 658 Chen, L., Fortier, D., McKenzie, J. M., and Sliger, M.: Impact of heat advection on the thermal
659 regime of roads built on permafrost, *Hydrol. Process.*, 34, 1647–1664,
660 <https://doi.org/10.1002/hyp.13688>, 2020.
- 661 Cheng, G. and Wu, T.: Responses of permafrost to climate change and their environmental
662 significance, Qinghai-Tibet Plateau, *J. Geophys. Res. Earth Surf.*, 112,
663 <https://doi.org/10.1029/2006JF000631>, 2007.
- 664 Coon, E. T., David Moulton, J., and Painter, S. L.: Managing complexity in simulations of land
665 surface and near-surface processes, *Environ. Model. Softw.*, 78, 134–149,
666 <https://doi.org/10.1016/j.envsoft.2015.12.017>, 2016.
- 667 Coon, E. T., Moulton, J. D., Kikinzon, E., Berndt, M., Manzini, G., Garimella, R., Lipnikov, K.,
668 and Painter, S. L.: Coupling surface flow and subsurface flow in complex soil structures using



- 669 mimetic finite differences, *Adv. Water Resour.*, 144, 103701,
670 <https://doi.org/10.1016/j.advwatres.2020.103701>, 2020.
- 671 Coon, E. T., Berndt, M., Jan, A., Svyatsky, D., Atchley, A. L., Kikinzon, E., Harp, D. R.,
672 Manzini, G., Shelef, E., Lipnikov, K., Garimella, R., Xu, C., Moulton, D., Karra, S., Painter, S.
673 L., Jafarov, E., and Molins, S.: Advanced Terrestrial Simulator. U.S. Department of Energy,
674 USA. Version 1.2. DOI: 10.11578/dc.20190911.1, 2021.
- 675 Dall’Amico, M., Endrizzi, S., Gruber, S., and Rigon, R.: A robust and energy-conserving model
676 of freezing variably-saturated soil, *The Cryosphere*, 5, 469–484, [https://doi.org/10.5194/tc-5-](https://doi.org/10.5194/tc-5-469-2011)
677 469-2011, 2011.
- 678 Dearborn, K. D., Wallace, C. A., Patankar, R., and Baltzer, J. L.: Permafrost thaw in boreal
679 peatlands is rapidly altering forest community composition, *J. Ecol.*, 109, 1452–1467,
680 <https://doi.org/10.1111/1365-2745.13569>, 2021.
- 681 Devoie, É. G. and Craig, J. R.: A Semianalytical Interface Model of Soil Freeze/Thaw and
682 Permafrost Evolution, *Water Resour. Res.*, 56, e2020WR027638,
683 <https://doi.org/10.1029/2020WR027638>, 2020.
- 684 Endrizzi, S., Gruber, S., Dall’Amico, M., and Rigon, R.: GEOTop 2.0: simulating the combined
685 energy and water balance at and below the land surface accounting for soil freezing, snow cover
686 and terrain effects, *Geosci. Model Dev.*, 7, 2831–2857, [https://doi.org/10.5194/gmd-7-2831-](https://doi.org/10.5194/gmd-7-2831-2014)
687 2014, 2014.
- 688 Fortier, D., Allard, M., and Shur, Y.: Observation of rapid drainage system development by
689 thermal erosion of ice wedges on Bylot Island, Canadian Arctic Archipelago, *Permafr. Periglac.*
690 *Process.*, 18, 229–243, <https://doi.org/10.1002/ppp.595>, 2007.
- 691 Godin, E., Fortier, D., and Coulombe, S.: Effects of thermo-erosion gullying on hydrologic flow
692 networks, discharge and soil loss, *Environ. Res. Lett.*, 9, 105010, [https://doi.org/10.1088/1748-](https://doi.org/10.1088/1748-9326/9/10/105010)
693 9326/9/10/105010, 2014.
- 694 Gottardi, G. and Venutelli, M.: A control-volume finite-element model for two-dimensional
695 overland flow, *Adv. Water Resour.*, 16, 277–284, [https://doi.org/10.1016/0309-1708\(93\)90019-](https://doi.org/10.1016/0309-1708(93)90019-C)
696 C, 1993.
- 697 Harp, D. R., Zlotnik, V., Abolt, C. J., Busey, B., Avendaño, S. T., Newman, B. D., Atchley, A.
698 L., Jafarov, E., Wilson, C. J., and Bennett, K. E.: New insights into the drainage of inundated
699 ice-wedge polygons using fundamental hydrologic principles, *The Cryosphere*, 15, 4005–4029,
700 <https://doi.org/10.5194/tc-15-4005-2021>, 2021.
- 701 Hinzman, L., Busey, B., Cable, W., and Romanovsky, V.: Surface Meteorology, Utqiagvik
702 (Barrow), Alaska, Area A, B, C and D, Ongoing from 2012, Next Generation Ecosystem
703 Experiments Arctic Data Collection, Oak Ridge National Laboratory, U.S. Department of
704 Energy, Oak Ridge, Tennessee, USA. Dataset accessed on October 10, 2021 at
705 <https://doi.org/10.5440/1164893>, 2014.
- 706 Hjort, J., Karjalainen, O., Aalto, J., Westermann, S., Romanovsky, V. E., Nelson, F. E.,
707 Etzelmüller, B., and Luoto, M.: Degrading permafrost puts Arctic infrastructure at risk by mid-
708 century, *Nat. Commun.*, 9, 5147, <https://doi.org/10.1038/s41467-018-07557-4>, 2018.
- 709 Hugelius, G., Strauss, J., Zubrzycki, S., Harden, J. W., Schuur, E. a. G., Ping, C.-L.,



- 710 Schirrmeister, L., Grosse, G., Michaelson, G. J., Koven, C. D., O'Donnell, J. A., Elberling, B.,
711 Mishra, U., Camill, P., Yu, Z., Palmtag, J., and Kuhry, P.: Estimated stocks of circumpolar
712 permafrost carbon with quantified uncertainty ranges and identified data gaps, *Biogeosciences*,
713 11, 6573–6593, <https://doi.org/10.5194/bg-11-6573-2014>, 2014.
- 714 Jafarov, E. E., Coon, E. T., Harp, D. R., Wilson, C. J., Painter, S. L., Atchley, A. L., and
715 Romanovsky, V. E.: Modeling the role of preferential snow accumulation in through talik
716 development and hillslope groundwater flow in a transitional permafrost landscape, *Environ.*
717 *Res. Lett.*, 13, 105006, <https://doi.org/10.1088/1748-9326/aadd30>, 2018.
- 718 Jan, A., Coon, E. T., Painter, S. L., Garimella, R., and Moulton, J. D.: An intermediate-scale
719 model for thermal hydrology in low-relief permafrost-affected landscapes, *Comput. Geosci.*, 22,
720 163–177, <https://doi.org/10.1007/s10596-017-9679-3>, 2018.
- 721 Jan, A., Coon, E. T., and Painter, S. L.: Evaluating integrated surface/subsurface permafrost
722 thermal hydrology models in ATS (v0.88) against observations from a polygonal tundra site,
723 *Geosci. Model Dev.*, 13, 2259–2276, <https://doi.org/10.5194/gmd-13-2259-2020>, 2020.
- 724 Jorgenson, M. T., Racine, C. H., Walters, J. C., and Osterkamp, T. E.: Permafrost Degradation
725 and Ecological Changes Associated with a Warming Climate in Central Alaska, *Clim. Change*,
726 48, 551–579, <https://doi.org/10.1023/A:1005667424292>, 2001.
- 727 Karra, S., Painter, S. L., and Lichtner, P. C.: Three-phase numerical model for subsurface
728 hydrology in permafrost-affected regions (PFLOTRAN-ICE v1.0), *The Cryosphere*, 8, 1935–
729 1950, <https://doi.org/10.5194/tc-8-1935-2014>, 2014.
- 730 Kurylyk, B. L. and Watanabe, K.: The mathematical representation of freezing and thawing
731 processes in variably-saturated, non-deformable soils, *Adv. Water Resour.*, 60, 160–177,
732 <https://doi.org/10.1016/j.advwatres.2013.07.016>, 2013.
- 733 Kurylyk, B. L., MacQuarrie, K. T. B., and McKenzie, J. M.: Climate change impacts on
734 groundwater and soil temperatures in cold and temperate regions: Implications, mathematical
735 theory, and emerging simulation tools, *Earth-Sci. Rev.*, 138, 313–334,
736 <https://doi.org/10.1016/j.earscirev.2014.06.006>, 2014.
- 737 Luethi, R., Phillips, M., and Lehning, M.: Estimating Non-Conductive Heat Flow Leading to
738 Intra-Permafrost Talik Formation at the Ritigraben Rock Glacier (Western Swiss Alps), *Permafr.*
739 *Periglac. Process.*, 28, 183–194, <https://doi.org/10.1002/ppp.1911>, 2017.
- 740 McKenzie, J. M. and Voss, C. I.: Permafrost thaw in a nested groundwater-flow system,
741 *Hydrogeol. J.*, 21, 299–316, <https://doi.org/10.1007/s10040-012-0942-3>, 2013.
- 742 McKenzie, J. M., Voss, C. I., and Siegel, D. I.: Groundwater flow with energy transport and
743 water–ice phase change: numerical simulations, benchmarks, and application to freezing in peat
744 bogs, *Adv. Water Resour.*, 30, 966–983, <https://doi.org/10.1016/j.advwatres.2006.08.008>, 2007.
- 745 NEON (National Ecological Observatory Network): 2D wind speed and direction
746 (DP1.00001.001): RELEASE-2021, <https://doi.org/10.48443/s9ya-zc81>, 2021. Dataset accessed
747 from <https://data.neonscience.org> on October 10, 2021.
- 748 Nixon, J. F.: The Role of Convective Heat Transport in the Thawing of Frozen Soils, *Can.*
749 *Geotech. J.*, 12, 425–429, <https://doi.org/10.1139/t75-046>, 1975.
- 750 Noh, J.-H., Lee, S.-R., and Park, H.: Prediction of cryo-SWCC during freezing based on pore-



- 751 size distribution, *Int. J. Geomech.*, 12, 428–438, [https://doi.org/10.1061/\(ASCE\)GM.1943-5622.0000134](https://doi.org/10.1061/(ASCE)GM.1943-5622.0000134), 2012.
- 753 O'Connor, M. T., Cardenas, M. B., Ferencz, S. B., Wu, Y., Neilson, B. T., Chen, J., and Kling,
754 G. W.: Empirical Models for Predicting Water and Heat Flow Properties of Permafrost Soils,
755 *Geophys. Res. Lett.*, 47, e2020GL087646, <https://doi.org/10.1029/2020GL087646>, 2020.
- 756 Painter, S. L.: Three-phase numerical model of water migration in partially frozen geological
757 media: model formulation, validation, and applications, *Comput. Geosci.*, 15, 69–85,
758 <https://doi.org/10.1007/s10596-010-9197-z>, 2011.
- 759 Painter, S. L. and Karra, S.: Constitutive Model for Unfrozen Water Content in Subfreezing
760 Unsaturated Soils, *Vadose Zone J.*, 13, vzt2013.04.0071,
761 <https://doi.org/10.2136/vzt2013.04.0071>, 2014.
- 762 Painter, S. L., Coon, E. T., Atchley, A. L., Berndt, M., Garimella, R., Moulton, J. D., Svyatskiy,
763 D., and Wilson, C. J.: Integrated surface/subsurface permafrost thermal hydrology: Model
764 formulation and proof-of-concept simulations: integrated permafrost thermal hydrology, *Water
765 Resour. Res.*, 52, 6062–6077, <https://doi.org/10.1002/2015WR018427>, 2016.
- 766 Riseborough, D., Shiklomanov, N., Etzelmüller, B., Gruber, S., and Marchenko, S.: Recent
767 advances in permafrost modelling, *Permafrost Periglacial Process.*, 19, 137–156,
768 <https://doi.org/10.1002/ppp.615>, 2008.
- 769 Rowland, J. C., Travis, B. J., and Wilson, C. J.: The role of advective heat transport in talik
770 development beneath lakes and ponds in discontinuous permafrost, *Geophys. Res. Lett.*, 38,
771 <https://doi.org/10.1029/2011GL048497>, 2011.
- 772 Sjöberg, Y., Coon, E., K. Sannel, A. B., Pannetier, R., Harp, D., Frampton, A., Painter, S. L., and
773 Lyon, S. W.: Thermal effects of groundwater flow through subarctic fens: A case study based on
774 field observations and numerical modeling, *Water Resour. Res.*, 52, 1591–1606,
775 <https://doi.org/10.1002/2015WR017571>, 2016.
- 776 Stuurup, J. C., van der Zee, S. E. A. T. M., Voss, C. I., and French, H. K.: Simulating water and
777 heat transport with freezing and cryosuction in unsaturated soil: Comparing an empirical, semi-
778 empirical and physically-based approach, *Adv. Water Resour.*, 149, 103846,
779 <https://doi.org/10.1016/j.advwatres.2021.103846>, 2021.
- 780 Sugimoto, A., Yanagisawa, N., Naito, D., Fujita, N., and Maximov, T. C.: Importance of
781 permafrost as a source of water for plants in east Siberian taiga, *Ecol. Res.*, 17, 493–503,
782 <https://doi.org/10.1046/j.1440-1703.2002.00506.x>, 2002.
- 783 Tesi, T., Muschitiello, F., Smittenberg, R. H., Jakobsson, M., Vonk, J. E., Hill, P., Andersson,
784 A., Kirchner, N., Noormets, R., Dudarev, O., Semiletov, I., and Gustafsson, Ö.: Massive
785 remobilization of permafrost carbon during post-glacial warming, *Nat. Commun.*, 7, 13653,
786 <https://doi.org/10.1038/ncomms13653>, 2016.
- 787 Thornton, M. M., Wei, Y., Thornton, P. E., Shrestha, R., Kao, S., and Wilson, B. E.: Daymet:
788 Station-Level Inputs and Cross-Validation Result for North America, Version 4,
789 <https://doi.org/10.3334/ORNLDAAAC/1850>, 2020.
- 790 Thornton, P. E., Shrestha, R., Thornton, M., Kao, S.-C., Wei, Y., and Wilson, B. E.: Gridded
791 daily weather data for North America with comprehensive uncertainty quantification, *Sci. Data*,



- 792 8, 190, <https://doi.org/10.1038/s41597-021-00973-0>, 2021.
- 793 Van Genuchten, M. T.: A Closed-form Equation for Predicting the Hydraulic Conductivity of
794 Unsaturated Soils, *Soil Sci. Soc. Am. J.*, 44, 892–898,
795 <https://doi.org/10.2136/sssaj1980.03615995004400050002x>, 1980.
- 796 Viterbo, P., Beljaars, A., Mahfouf, J.-F., and Teixeira, J.: The representation of soil moisture
797 freezing and its impact on the stable boundary layer, *Q. J. R. Meteorol. Soc.*, 125, 2401–2426,
798 <https://doi.org/10.1002/qj.49712555904>, 1999.
- 799 Walvoord, M. A. and Kurylyk, B. L.: Hydrologic Impacts of Thawing Permafrost—A Review,
800 *Vadose Zone J.*, 15, <https://doi.org/10.2136/vzj2016.01.0010>, 2016.
- 801 Wasantha Lal, A. M.: Weighted Implicit Finite-Volume Model for Overland Flow, *J. Hydraul.*
802 *Eng.*, 124, 941–950, [https://doi.org/10.1061/\(ASCE\)0733-9429\(1998\)124:9\(941\)](https://doi.org/10.1061/(ASCE)0733-9429(1998)124:9(941)), 1998.
- 803 Weismüller, J., Wollschläger, U., Boike, J., Pan, X., Yu, Q., and Roth, K.: Modeling the thermal
804 dynamics of the active layer at two contrasting permafrost sites on Svalbard and on the Tibetan
805 Plateau, *The Cryosphere*, 5, 741–757, <https://doi.org/10.5194/tc-5-741-2011>, 2011.
- 806 Westermann, S., Langer, M., Boike, J., Heikenfeld, M., Peter, M., Etzelmüller, B., and Krinner,
807 G.: Simulating the thermal regime and thaw processes of ice-rich permafrost ground with the
808 land-surface model CryoGrid 3, *Geosci. Model Dev.*, 9, 523–546, <https://doi.org/10.5194/gmd-9-523-2016>, 2016.
- 810 Zhang, T., Barry, R. G., Knowles, K., Heginbottom, J. A., and Brown, J.: Statistics and
811 characteristics of permafrost and ground-ice distribution in the Northern Hemisphere, *Polar*
812 *Geogr.*, 31, 47–68, <https://doi.org/10.1080/10889370802175895>, 2008.
- 813